

Article

Performance and Formula Optimization of Graphene-Modified Tungsten Carbide Coating to Improve Adaptability to High-Speed Fluid Flow in Wellbore

Minsheng Wang ^{1,2} , Lingchao Xuan ^{1,2}, Lei Wang ^{1,2} and Jiangshuai Wang ^{1,3,*} 

- ¹ State Key Laboratory of Shale Oil and Gas Enrichment Mechanisms and Effective Development, Beijing 100083, China; wangms.sripe@sinopec.com (M.W.); xuanlc.sripe@sinopec.com (L.X.); wanglei8.sripe@sinopec.com (L.W.)
- ² Sinopec Research Institute of Petroleum Engineering Co., Ltd., Beijing 100020, China
- ³ School of Petroleum and Gas Engineering, Changzhou University, Changzhou 213164, China
- * Correspondence: wjs125126@163.com

Abstract: In order to improve the erosion resistance of steel PDC (Polycrystalline Diamond Compact) bit under high-speed fluid flow conditions underground, it is necessary to develop a high-performance erosion-resistant coating. In this paper, laser cladding was used to prepare the new coating by modifying tungsten carbide with graphene. And the effects of tungsten carbide content and graphene content on the coating performance have been thoroughly studied and analyzed to obtain the optimal covering layer. The research results indicate that, for new coatings, 60% tungsten carbide and 0.3% graphene are the optimal ratios. After adding tungsten carbide, the hardness has significantly improved. However, when the tungsten carbide content further increases more than 30%, the increase in hardness is limited. In addition, when the content of graphene is more than 0.3%, the branched structure becomes thicker. In detail, this is a phenomenon where the segregation of Cr, Si, and W becomes very obvious again, and the segregation of Fe occurs at the Ni enrichment site. The research results contribute to the development and optimization of high-quality erosion-resistant coatings under the high-speed flow conditions in wellbore. These are of great significance for improving the efficiency of oil and gas exploration and development.

Keywords: PDC drill bit; coating; optimization; tungsten carbide; graphene



Citation: Wang, M.; Xuan, L.; Wang, L.; Wang, J. Performance and Formula Optimization of Graphene-Modified Tungsten Carbide Coating to Improve Adaptability to High-Speed Fluid Flow in Wellbore. *Processes* **2024**, *12*, 714. <https://doi.org/10.3390/pr12040714>

Academic Editor: Hyun Wook Jung

Received: 6 March 2024

Revised: 26 March 2024

Accepted: 28 March 2024

Published: 31 March 2024



Copyright: © 2024 by the authors. Licensee MDPI, Basel, Switzerland. This article is an open access article distributed under the terms and conditions of the Creative Commons Attribution (CC BY) license (<https://creativecommons.org/licenses/by/4.0/>).

1. Introduction

Energy security plays a decisive role in the stable operation and high-quality development of society [1,2]. In the process of oil and gas development and production, when the flow rate in the wellbore is large, the underground materials will be eroded, causing the operation to be unable to proceed smoothly and reducing the efficiency of oil and gas production. In order to improve the erosion resistance of steel PDC drill bits under high-speed fluid flow conditions underground, it is necessary to develop a high-performance erosion-resistant coating. It can greatly improve operational efficiency [3–5].

Under long-term operation or complex working conditions (such as composite wear [6] and mud erosion [7–9]), steel PDC bit may experience erosion and mud inclusion on the blade, especially in the main cutting section of the blade crown, which is prone to erosion. The impact force on the erosion area is relatively large, and the protective capacity of this area is relatively insufficient, greatly limiting the use of steel PDC bit. Laser cladding technology is commonly used for developing high-performance and high-quality coatings. Nickel-based alloy coatings are widely used in laser cladding processes because they are economical and have good self-lubricating performance and corrosion resistance [10,11]. Tungsten carbide has the characteristics of high hardness, high melting point, strong wear resistance, and corrosion resistance, and is usually used in a wide range of coating

materials [12–16]. Graphene has outstanding mechanical and thermal properties and two-dimensional sheet structure, which can also be used as coating material for laser cladding process [17,18]. It is necessary to use tungsten carbide and graphene as coating materials to prepare new coatings with good wear resistance and erosion resistance. For example, Zhan et al. [19] studied the basic properties of multi-layer graphene and its application in the industrial field. This is a very important aspect to utilize graphene to improve the performance of materials at high temperatures. Jagannadham [20] developed a tungsten-graphene-layered film by the deposition of tungsten film by magnetron sputtering on the graphene-covered copper foils. This product has high performance and high temperature resistance. Then, Chen et al. [21] developed graphene nanoplatelet-supported tungsten carbide nitride nanocomposites that were prepared via an in situ solid-state approach. This nanocomposite catalyzes the hydrogen evolution reaction with very low overpotential and is stable operating for at least 300 h in harsh acidic conditions. Recently, Xuan and Wang [22] developed a new type of high hardness coating for improving drill bit stability in unconventional oil and gas development. Moreover, the hardness of coatings under different cladding processes has been studied and explained.

Although scholars have already completed some studies, research on the development and optimization of modified tungsten carbide coatings is very limited. This is a coating that can greatly improve the erosion resistance of PDC drill bits. Therefore, in this paper, laser cladding was used to prepare the new coating by modifying tungsten carbide with graphene. And the effects of tungsten carbide content and graphene content on the coating performance have been thoroughly studied and analyzed to obtain the optimal covering layer. The research results contribute to the development and optimization of high-quality erosion-resistant coatings under the high-speed flow conditions in wellbore.

2. Experimental Materials, Equipment, and Methods

2.1. Experimental Materials

The experimental materials of this laser cladding project mainly include base plate and powder. The base plate is made of Q235 steel (Figure 1), and the powder includes Ni60A powder, tungsten carbide (WC) powder, and single-layer graphene.



Figure 1. Q235 steel base plate.

Specifically, Q235 steel composition is shown in Table 1.

Table 1. Q235 chemical composition table.

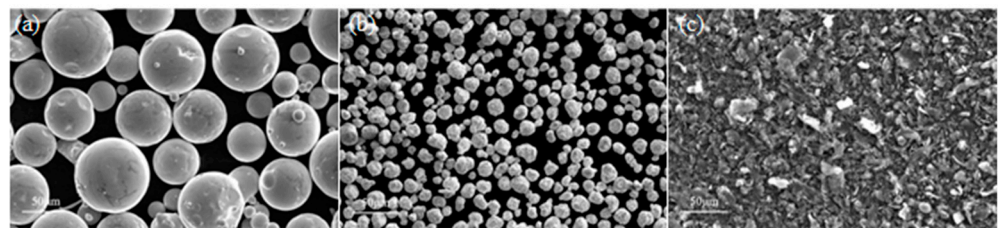
Element	Fe	C	Si	Mn	Cr	Ni	Cu
Component (wt.%)	Bal.	0.16	0.26	0.15	0.02	0.025	0.024

Ni60A powder composition is shown in Table 2.

Table 2. Chemical composition of Ni60A powder.

Element	Ni	Cr	Fe	Si	B	C	O
Component (wt.%)	Bal.	16.58	4.63	4.11	3.02	0.76	0.03

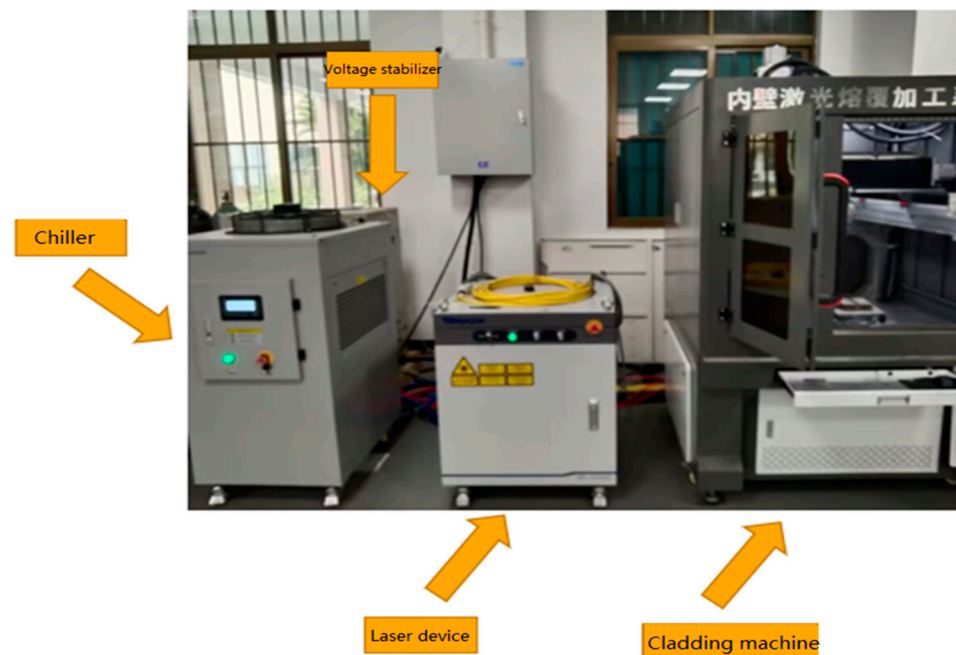
The micrographs of Ni60A powder, tungsten carbide powder, and graphene powder under SEM are as shown in Figure 2.

**Figure 2.** The SEM of the powder of (a) Ni60A, (b) WC, and (c) graphene.

From the powder SEM micrographs, it can be seen that Ni60A powder particles form a uniform, spherical powder, having good mobility, with less satellite powder around the powder; graphene powder has a typical lamellar form.

2.2. Experimental Equipment

Powder laser cladding equipment was used in the experiment. It can be seen in Figure 3.

**Figure 3.** Powder-laying laser cladding equipment.

The powder-spreading laser cladding equipment consists of four parts. Part I is a chiller. Part II is a voltage stabilizer. Part III is a laser device. Part IV is a cladding machine.

2.3. Experimental Methods

In summary, the process of preparing a new coating using laser cladding technology is shown in Figure 4.

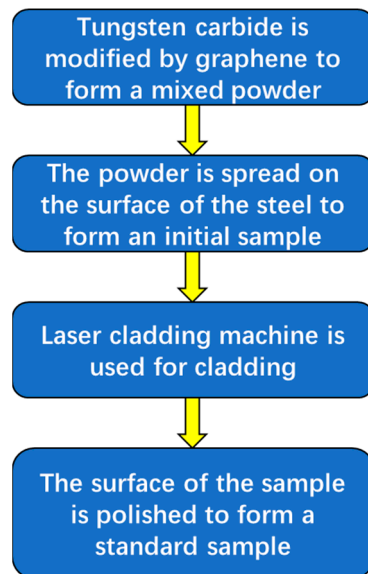


Figure 4. The process of using laser cladding technology to prepare a new coating.

The following important steps need to be completed before preparing the laser cladding coating.

Firstly, it is necessary to use graphene to modify tungsten carbide and form a mixed powder. In this process, it is necessary to add 5–10% dispersant, whose main component is sodium dodecylbenzene sulfonate. It can help to evenly mix various components and strengthen the organizational structure of the coating.

Then, 60 grit sandpaper is used to polish the Q235 steel substrate to remove surface oxide film and increase surface roughness. It is beneficial for improving the adhesion between the substrate and the powder during melting.

Finally, the mixed powder sample should be placed in a vacuum drying oven for 2 h. Figure 5 shows the experimental sample after powder spreading.

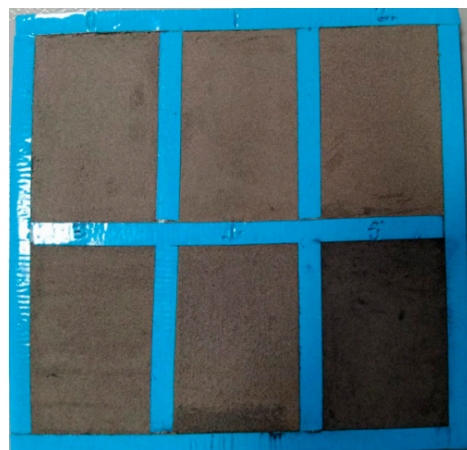


Figure 5. The experimental sample after powder spreading.

After powder spreading, laser cladding machine is used to melt different areas. Then, the sample is cut into standard specimens for experimental testing by wire cutting. At the same time, the surface of the sample needs to be polished. Figure 6 shows the experimental sample after polishing.



Figure 6. The experimental sample after polishing.

Next, the following three types of tests need to be conducted on the standard samples. Through these three tests, hardness data and surface morphology under different conditions can be obtained, which are directly related to the erosion resistance of the coating.

(1) Hardness test

The reference standard is GB/T 230.1-2018 [23]. The hardness tester is used to test the microhardness of the coating section. The four-point-measurement method is used to measure the hardness. Due to the subjectivity of hardness measurement, in order to ensure the accuracy of the average hardness results obtained, 10 points are randomly selected from each of the two planes parallel and perpendicular to the laser walkway on the same sample for testing. All 20 points are sorted from high to low, and the average and standard deviation are calculated after removing the maximum and minimum values.

(2) XRD Test

The reference standard is YB/T 5336-2006 [24]. The sample was tested by X-ray diffractometer goniometer. Then, the Jade6.5 software was used to analyze the test results.

(3) Microstructure observation

The reference standard is ISO17639-2003 [25]. Scanning electron microscopy was used to observe the microstructure. Then, EDS testing was used to determine the composition and distribution of the coating elements.

3. Experiment Results and Discussion on the Influence of Tungsten Carbide Content on Coating Performance

This project conducted pre-experiments to determine the experimental parameters and plan before work. Parameters are shown in Table 3. According to the relevant literature, WC (tungsten carbide) content often has a significant impact on the hardness of the coating at a high level, and trace amounts of graphene can demonstrate its role. Therefore, in the pre-experimental stage, it was decided to use Ni60A + 30% WC + 0.1% graphene mixed powder to prepare the coating layer under different parameters, as the hardness of the coating layer can be used to preliminarily determine the material's resistance to mud erosion. Therefore, parameter selection is based on hardness. Specifically, the laser power is selected as 800 W, 1200 W, 1600 W, and 2000 W, as shown in the Table 4.

The obtained hardness result is as follows:

According to the hardness test results, it can be seen that the average hardness values of the coatings obtained at 800 W and 1200 W are not significantly different. However, as the power increases, the hardness of the coatings obtained at 1200 W, 1600 W, and 2000 W

decreases significantly. Based on the above results, the cladding parameters determined in this pre-experiment are as follows: laser spot of 4 mm, laser power of 1200 W, speed of 0.35 m/min, overlap rate of 50%, and protective gas at 15 L/min.

For this project, the research on the matching cladding process of the new tungsten carbide coating is as follows: the cladding parameters determined in the previous section first melted the pure Ni60A powder coating, and then prepared the coating with WC/Ni60A mixed powder with WC mass fractions of 10%, 20%, 30%, 40%, 50%, and 60%.

The hardness test results of WC/Ni60A coatings with different WC contents are shown in Table 5. It can be seen from the table that, when WC is not added, the average hardness of Ni60A coatings is only 753.3 HV. However, after adding WC, the hardness has significantly improved, especially when the WC content is 10% and 20%, the average hardness has increased by 13.3% and 32.6%, respectively. As the WC content continues to increase, the average hardness also increases, but the increase is smaller than the first 20%.

Table 3. Pre-experimental parameters.

Powder	Speed (m/min)	Light Spot (mm)	Overlapping Ratio	Shielding Gas (L/min)
Ni60A + 30% WC +0.1% graphene	0.35	4	50%	15

Table 4. Ni60A + 30% WC + 0.1% graphene hardness results at different power levels.

Laser power (W)	800	1200	1600	2000
Average hardness (HV)	1063.3	1086.2	732.6	526.8

Table 5. Hardness of coatings with different tungsten carbide contents.

WC content (wt.%)	0%	10%	20%	30%	40%	50%	60%
Average hardness (HV)	753.3	853.3	998.5	1000.3	1019.2	1022.1	1075.9
Standard deviation	78.3	58.2	70.5	72.3	112.6	79.6	52.0

The hardness distribution of the cross-section of the cladding layer is shown in Figure 7. The hardness distribution area can be divided into the cladding layer zone, fusion zone, and heat-affected zone. The cladding layer zone has the highest hardness, and the fusion zone belongs to the transition zone, where the hardness begins to decrease. It can be seen that the hardness value of the cladding layer zone does not change much, while the hardness of the fusion zone rapidly decreases, indicating that the fusion zone is relatively narrow.

Figure 8 shows the SEM image of the Ni60A coating, which shows a relatively uniform distribution of Fe and Si, while Cr exhibits significant segregation and aggregation in blocks or strips. Ni is widely distributed throughout the coating due to its highest content in Ni60A powder.

The EDS data obtained from point A and point B at the Cr enrichment site are shown in Table 6. It can be observed that there is a significant difference in the mass fractions of Cr and Ni between the two sites, while the composition of Si and Fe is not significantly different. It can be seen that the content of Ni is the highest among the two points, which is because the proportion of Ni in Ni60A powder is the highest. According to the combination of XRD analysis results and EDS analysis results, it can be concluded that the main components of Cr enrichment are Cr₃C₂ and M₂₃C₆, while the remaining areas are mainly solid solutions of 7-Ni, Ni₃Fe, M₂₃C₆, and Fe₃C.

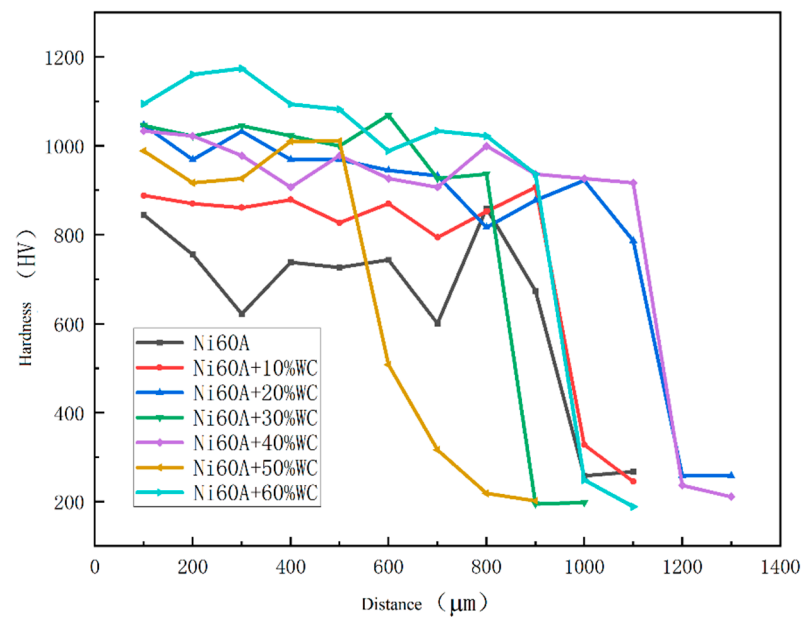


Figure 7. Microhardness of Ni60A coating with different mass fractions of tungsten carbide.

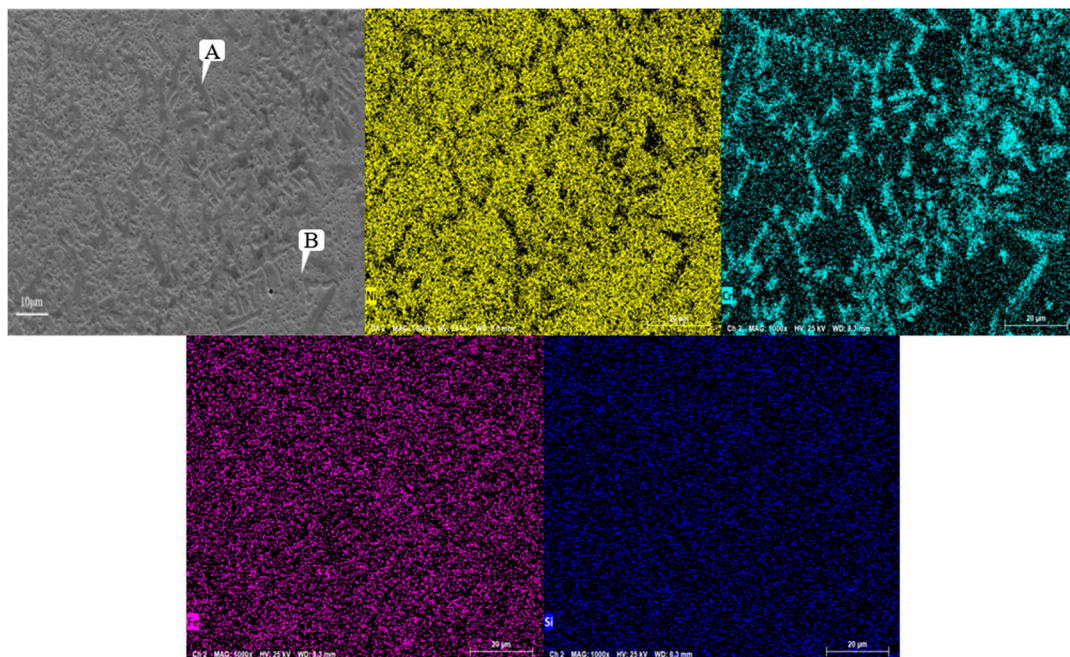


Figure 8. Microstructure and morphology of Ni60A coating.

Table 6. Microstructure and composition of Ni60A coating at different positions (mass fraction, %).

Position	Ni	Cr	Fe	Si
A	55.19	35.70	4.89	4.22
B	82.12	8.73	5.11	4.04

Figure 9 shows the SEM image of Ni60A + 20% WC coating. Comparing with Figure 8, it can be seen that, after the addition of WC, obvious snowflake-like and branch-like structures are formed at the Cr segregation area, resulting in significant Si element segregation in the obtained coating. From the EDS results at points C and D in Table 7, it can be seen that Si and W exhibit significant segregation in snowflake-like dendrites. As shown in

Figure 10, compared to the Ni60A coating, the Ni60A + 20% WC coating increases WC, W_2C , WSi_2 , W, and C. Due to the melting point of WC being 2870 °C, the melting points of Ni, Fe, and Cr are 1453 °C, 1538 °C, and 1907 °C, respectively. For low-speed laser cladding, excessive heat input can cause a certain amount of WC particles to decompose into carbides, resulting in a decrease in WC particles. On the other hand, it can increase the convection and stirring time of the molten pool, resulting in uneven distribution of WC particles. Based on the XRD detection results, it can be seen that, during the melting process, WC partially decomposes into W and C due to heating, and some W will form WSi_2 with Si at high temperatures, resulting in significant segregation of Si. At the same time, due to the decarburization phenomenon of WC at high temperatures, some WC will be converted into W_2C . According to the theory of metal crystallization, due to the relatively high melting point of W and its compounds, the precipitated phase will first solidify during the cladding process, increasing the probability of non-uniform nucleation forming around it. Due to the much higher melting point of Cr than Ni, Cr and its compounds will first adhere to W and its compounds during the cladding process, which is manifested in SEM images as the segregation of Cr, Si, and W, forming snowflake-like and branch-like structures. At the same time, due to the randomness of the precipitation of W and its compounds, the distribution of W does not exhibit obvious segregation characteristics like Cr, but rather forms a feature of widespread distribution and partial segregation.

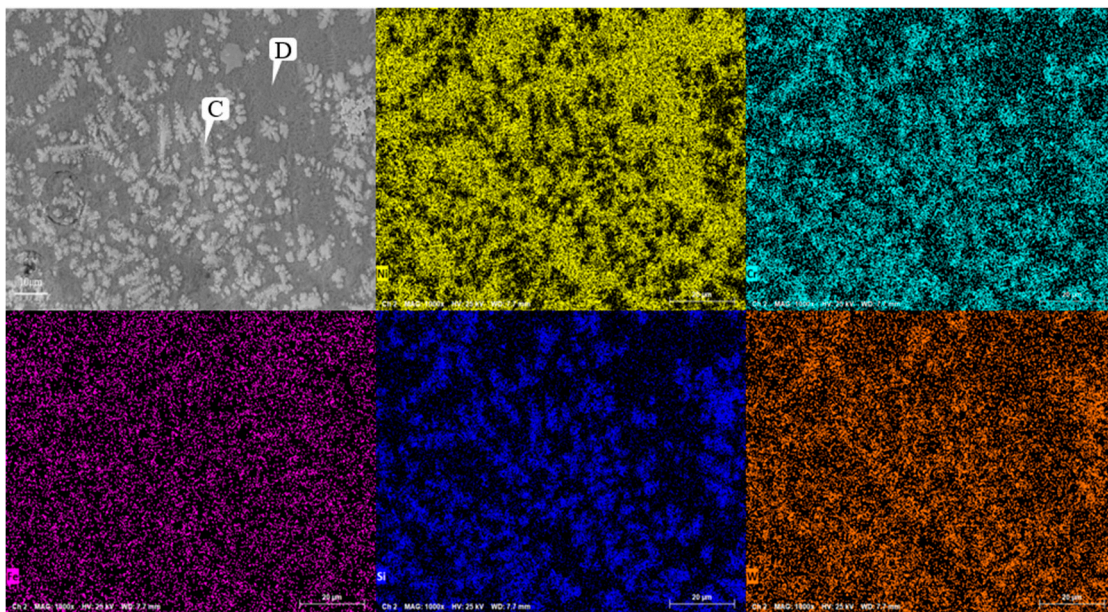


Figure 9. Microstructure of coating of Ni60A + 20% tungsten carbide.

Table 7. Microstructure and composition of coating of Ni60A + 20% tungsten carbide at different positions (mass fraction, %).

Position	Ni	Cr	Fe	Si	W
C	22.11	28.56	3.50	7.07	38.76
D	70.95	7.36	4.53	2.74	14.42

Figure 10 shows the SEM image of the Ni60A + 60% WC coating. Unlike the snowflake-like tissue of the Ni60A + 20% WC coating, needle-like interlaced tissue is formed in the majority of the areas at this time, while cluster-like tissue is formed in a small portion of the areas. Comparing with Figure 9, it can be seen that, as the mass fraction of WC in the powder increases, the segregation phenomenon of W and Si becomes more obvious, but the distribution of Cr appears more uniform. According to the EDS scanning results at

different positions of the Ni60A + 60% WC coating in Table 8, it can be seen that, when the proportion of WC in the powder is 60%, W is distributed throughout the coating, but segregation can still be clearly observed. The content difference of Si in different positions is very obvious, almost all of it exists in needle-like tissues. Therefore, it can be further determined that the main compound formed by Si in the coating is WSi_2 . According to the above, due to the attachment of Cr and its compounds to the growth of W and its compounds, the distribution of Cr elements will be more uniform as W content increases. Due to the fact that the proportion of Ni element in this mixed powder is less than W, the Ni distribution area under the microscopic morphology is cut into polygonal areas one-by-one. This can be seen in Figure 11. As the WC content in the powder increases, the peaks of Cr_3C_2 and W_2C in the Ni60A + 60% WC coating are enhanced compared to the Ni60A + 20% WC coating, while the peaks of $M_{23}C_6$ and WSi_2 are relatively reduced. This is because more WC decomposes to produce C, resulting in an increase in the proportion of C in the formed C compound. Therefore, Cr_3C_2 and W_2C increase, while $M_{23}C_6$ and WSi_2 are limited by the content of Fe and Si; thus, the proportion of WC in the powder increases. Its relative peak in XRD decreases.

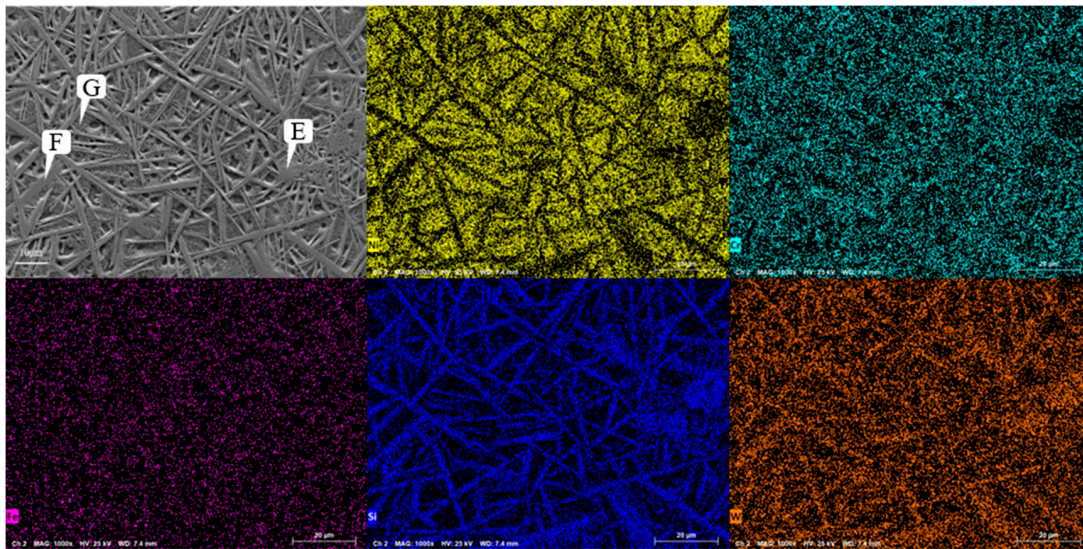


Figure 10. Microstructure of coating of Ni60A + 60% tungsten carbide.

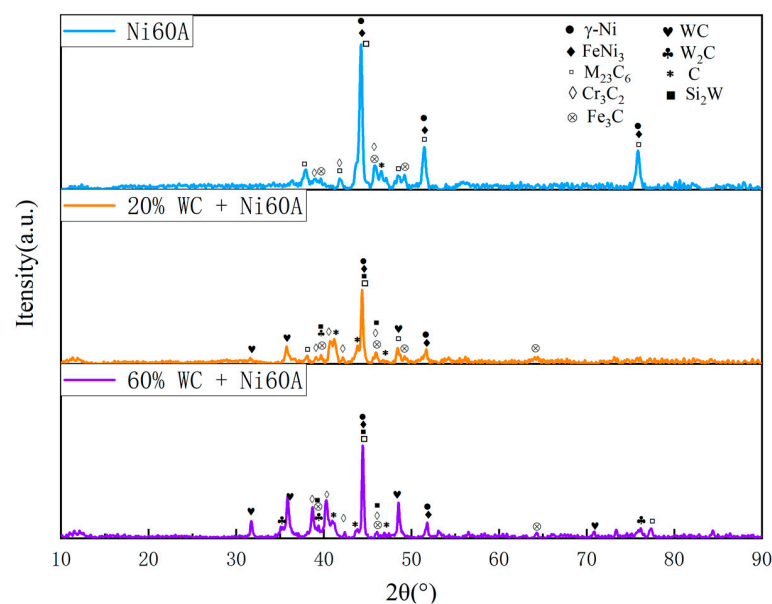


Figure 11. X-ray diffraction patterns of coatings of Ni60A with different tungsten carbide contents.

Table 8. Microstructure and composition of coating of Ni60A + 60% tungsten carbide at different positions (mass fraction, %).

Position	Ni	Cr	Fe	Si	W
E	3.99	2.47	1.78	10.94	80.82
F	7.64	11.19	2.03	6.69	72.45
G	56.99	7.47	2.49	0.73	37.27

4. Experiment Results and Discussion on the Influence of Graphene Content on Coating Performance

According to the research results in the previous section, Ni60A + 20% WC coating was selected to study the content of graphene, and the specific configuration of Ni60A + 20% WC + X% graphene (x = 0, 0.1, 0.3, 0.5) mixed powder was used for cladding experiment.

The experimental hardness test results are shown in Table 9, and the section hardness distribution is shown in Figure 12. It can be seen that, after adding graphene, the hardness of the coating is improved, and the measured hardness standard deviation is significantly reduced, indicating that, after adding graphene, the hardness difference between different areas of the coating becomes smaller. However, with the increase in graphene content, when the graphene content increases to 0.5%, compared to 0.3%, the average hardness decreases, and the hardness standard deviation increases, indicating that the hardness difference between different areas of the coating increases at this time. This is because the addition of excessive graphene will produce an aggregation phenomenon, resulting in uneven grain size and distribution in the microstructure, and the uniformity of coating hardness will be reduced.

Table 9. Average hardness of coatings with different graphene contents.

Graphene content (wt.%)	0%	0.1%	0.3%	0.5%
Average hardness	998.5	1021.7	1076.9	1036.1
Standard deviation	70.5	48.8	50.2	59.4

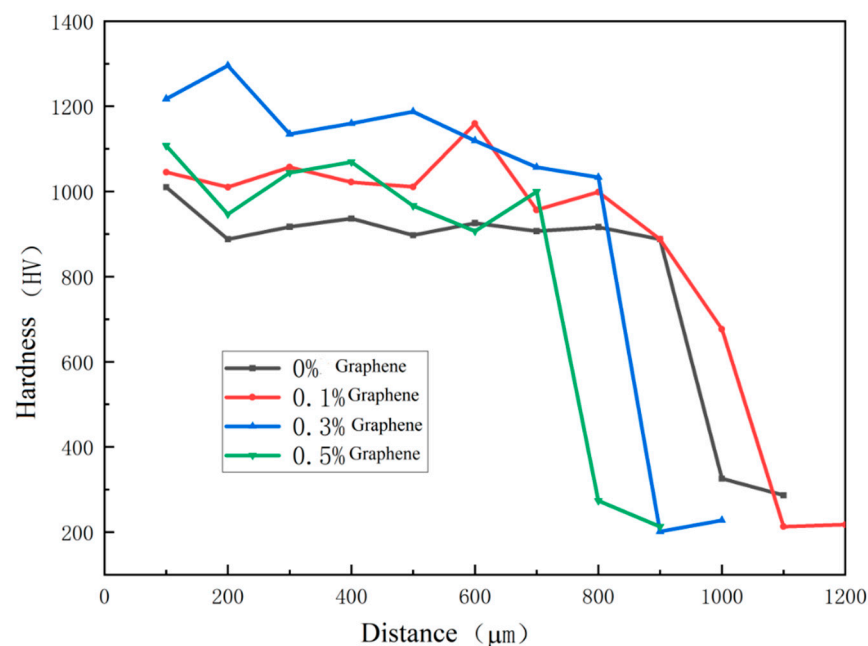
**Figure 12.** Microhardness of coatings containing different mass fractions of graphene.

Figure 13 shows the microstructure of the coating with different graphene contents. As mentioned earlier, when graphene is not added, it presents snowflake-like and branch-like

structures. With the increase in graphene content, the structure is refined first and then coarsened. When the content of graphene is 0.1%, the snowflake-like structure is dispersed into a smaller dot-like structure, while the branch-like structure becomes slenderer. And the part of the branch-like structure is dispersed and composed of a finer needle-like structure. According to the scanning results of the coating layer containing 0.1% graphene in Figure 14, it can be found that, although Cr, Si, and W are still segregated, compared to Figure 9, the segregation region is more evenly distributed in the whole coating layer. When the graphene content is 0.3%, according to the surface scan results in Figure 15, it can be found that the segregation of Cr, Si, and W is no longer obvious, especially the distribution of W and Cr in the whole region is relatively uniform. According to the analysis in Tables 10 and 11, the element composition comparison of different positions obtained from the coating containing 0.1% graphene and the coating containing 0.3% graphene shows that the element segregation has been significantly improved with the graphene content increasing to 0.3%. At the same time, with the increase in graphene, the coarse dendrites are replaced by fine dendrites [9], which makes the microstructure of the coating more fine, effectively reducing the porosity of the coating, and this coating has stronger erosion resistance. However, when the content of graphene was further increased to 0.5%, it can be observed from Figure 12 that the structure was not further refined but turned into a coarse strip structure. According to the scanning results of the coating layer containing 0.1% graphene in Figure 16, it can be found that not only did the segregation of Cr, Si, and W become very obvious again but also the segregation of Fe in Ni enrichment. Comparing the EDS results in Tables 6 and 12, it is found that, when 0.5% graphene is added to the coating, the element segregation phenomenon is more serious than that of the coating without graphene.

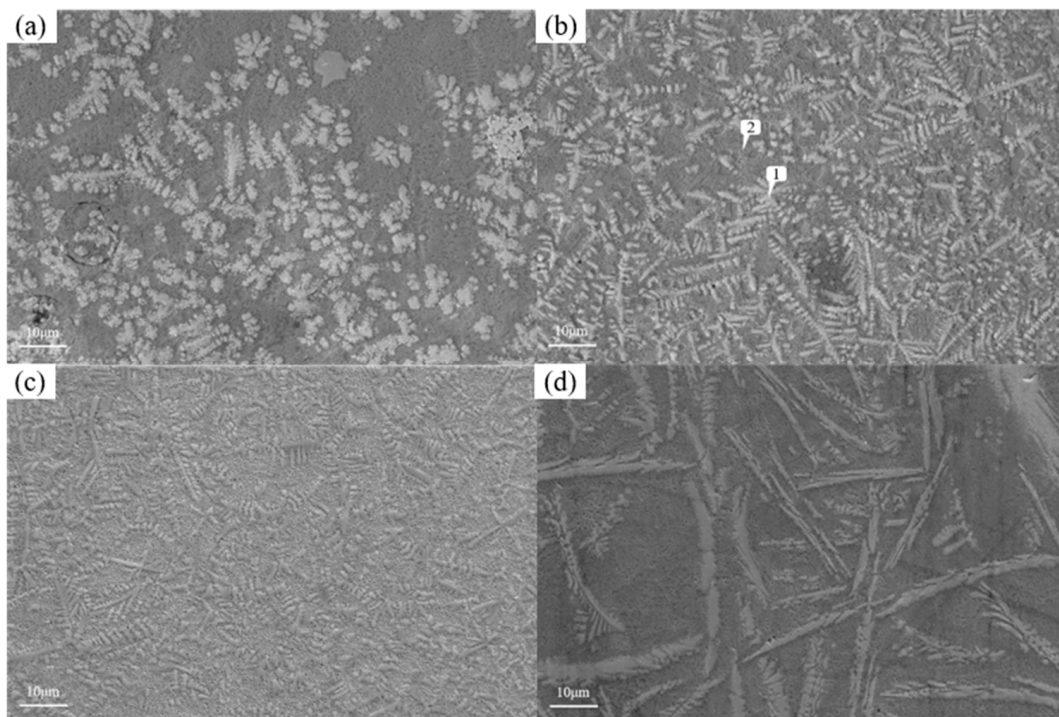


Figure 13. Microstructure of coatings with different graphene contents: (a) Ni60A + 20% tungsten carbide; (b) Ni60A + 20% tungsten carbide + 0.1% graphene; (c) Ni60A + 20% tungsten carbide + 0.3% graphene; and (d) Ni60A + 20% tungsten carbide + 0.5% graphene.

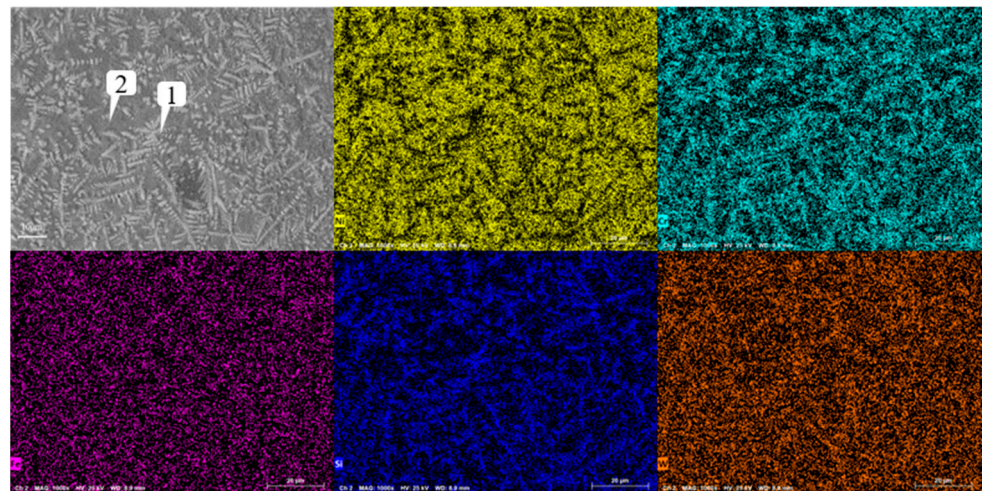


Figure 14. Analysis of scanning composition of coating Ni60A + 20% tungsten carbide + 0.1% graphene.

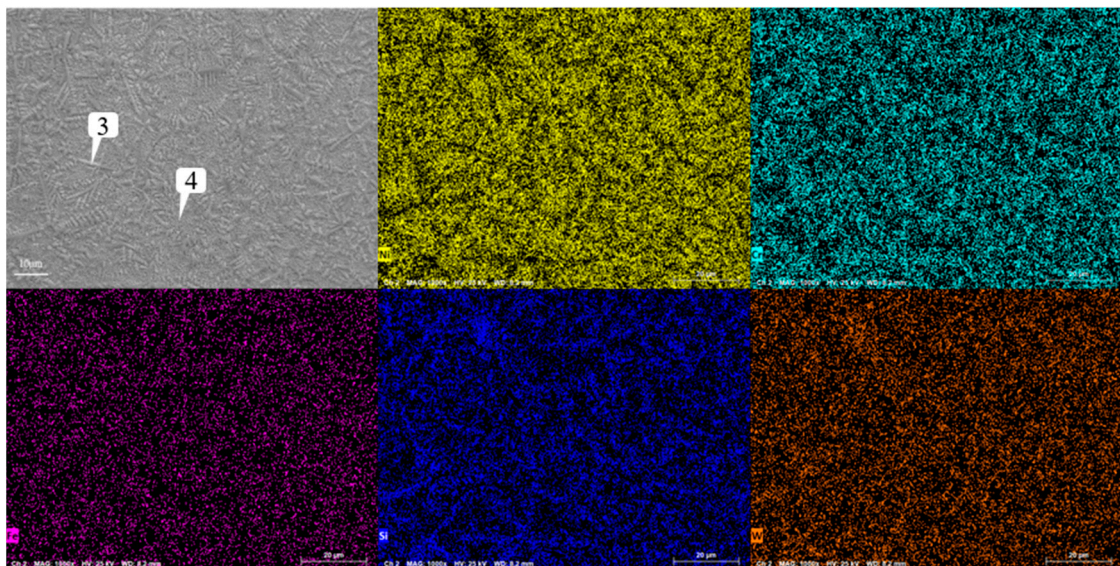


Figure 15. Analysis of scanning composition of coating Ni60A + 20% tungsten carbide + 0.3% graphene.

Table 10. Composition of coating Ni60A + 20% tungsten carbide + 0.1% graphene at different positions (mass fraction, %).

Position	Ni	Cr	Fe	Si	W
1	30.15	26.64	3.65	5.89	33.67
2	63.19	13.24	4.36	2.86	16.35

Table 11. Composition of coating Ni60A + 20% tungsten carbide + 0.3% graphene at different positions (mass fraction, %).

Position	Ni	Cr	Fe	Si	W
3	40.26	23.92	4.02	4.17	27.63
4	63.84	10.31	3.98	3.65	18.22

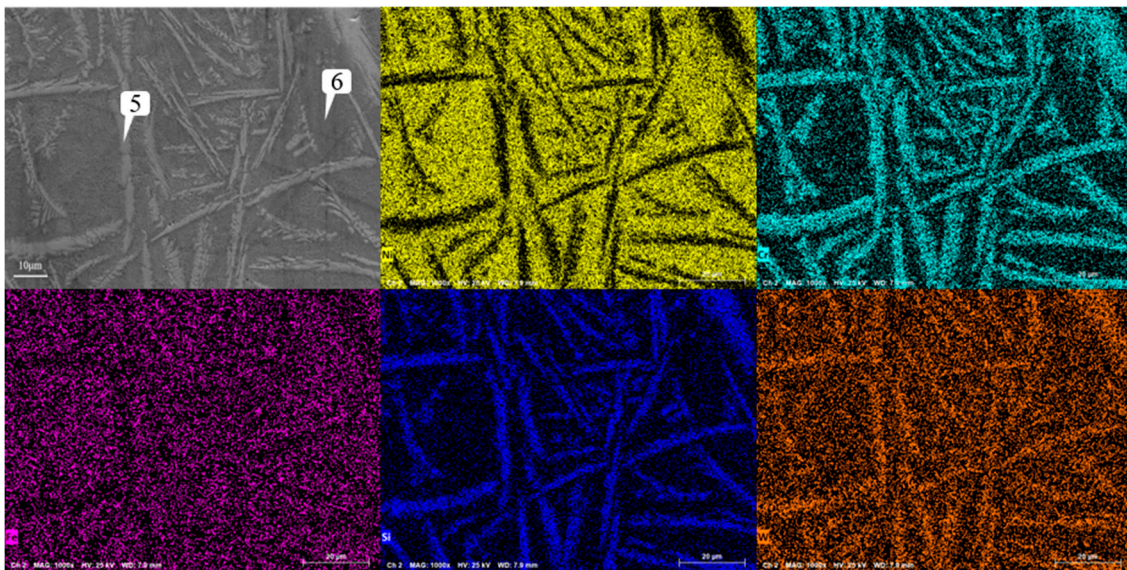


Figure 16. Analysis of scanning composition of coating Ni60A + 20% tungsten carbide + 0.5% graphene.

Table 12. Composition of coating Ni60A + 20% tungsten carbide + 0.5% graphene at different positions (mass fraction, %).

Position	Ni	Cr	Fe	Si	W
5	8.33	32.08	1.95	9.32	48.32
6	85.48	3.20	5.95	0.55	4.82

Figure 17 shows the X-ray diffraction patterns of WC/Ni60A composite coatings with different graphene contents. According to the XRD results, the addition of graphene has no obvious effect on the phase composition. With the addition of graphene, the content of different phases changes, which is specifically reflected in the change in peak intensity of different phases. After the addition of graphene, the peak intensity corresponding to Cr_3C_2 , WSi_2 , and W_2C increases compared to other phases. The above phases are hard phases, and the increase in their content helps to improve the hardness of the coating. When the content of graphene increases to 0.3%, it can be seen that the peak value of the generated phase in the XRD test results is relatively uniform. Combined with the above microscopic morphology analysis, a small amount of graphene can make the structure distribution more uniform and the grains more refined, so the hardness of the coating will be increased, and the hardness difference at different positions will be reduced. However, when the content of graphene increased to 0.5, it can be seen that the peak intensities of Cr_3C_2 and C in the XRD test increased significantly, but the peak intensities of W and its compounds and M_{23}C_6 decreased. It can be seen from Figure 16 that element segregation is intense at 0.5% graphene, which will lead to the uneven hardness distribution of the coating. The above analysis is consistent with the hardness test results in Table 9. Because graphene can increase the thermal conductivity of the coating, when there is a small amount of graphene in the coating, the thermal energy input by the laser can be dispersed to a certain extent, making the generated phase distribution uniform and reducing element segregation. However, due to the agglomeration characteristics of graphene, with the increase in graphene content, combined with its excellent thermal conductivity, the laser energy will accumulate during the cladding process, leading to the enrichment of the generated phase during precipitation.

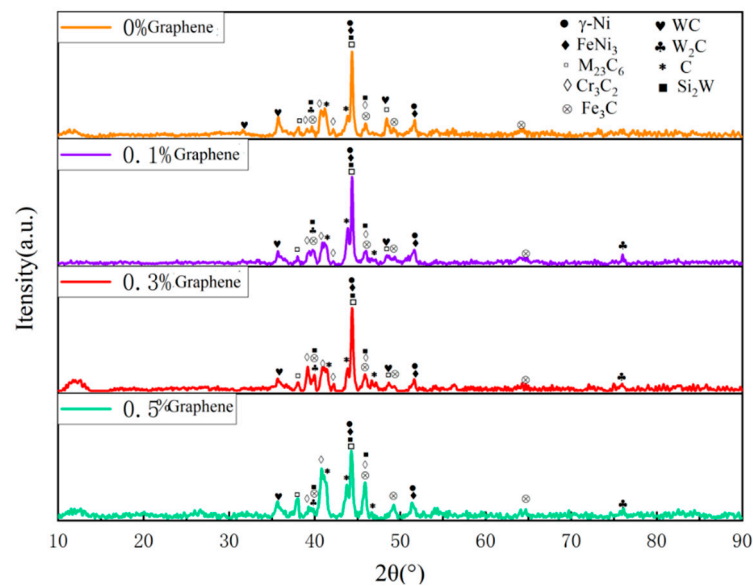


Figure 17. X-ray diffraction patterns of coating Ni60A + 20% tungsten carbide with different graphene contents.

5. Conclusions

The conclusions obtained in this paper are as follows:

- (1) For the new coatings, the hardness distribution area can be divided into the cladding layer zone, fusion zone, and heat-affected zone. The cladding layer zone has the highest hardness, and the fusion zone belongs to the transition zone, where the hardness begins to decrease.
- (2) For the new coatings, 60% tungsten carbide and 0.3% graphene are the optimal ratios. It can improve the erosion resistance of steel PDC drill bits under high-speed fluid flow conditions underground.
- (3) After adding WC, the hardness has significantly improved. However, when the WC content further increases to more than 30%, the increase in hardness is limited.
- (4) In addition, when the content of graphene is more than 0.3%, the branched structure becomes thicker. In detail, this is a phenomenon where the segregation of Cr, Si, and W becomes very obvious again, and the segregation of Fe occurs at the Ni enrichment site.

Author Contributions: Conceptualization, M.W. and J.W.; methodology, L.X. and J.W.; software, L.W.; validation, L.X., L.W. and J.W.; formal analysis, M.W.; investigation, M.W.; resources, M.W.; data curation, J.W.; writing—original draft preparation, L.X. and J.W.; writing—review and editing, M.W. and J.W.; visualization, L.X.; supervision, M.W. and L.X.; project administration, M.W. and J.W.; funding acquisition, M.W. and J.W. All authors have read and agreed to the published version of the manuscript.

Funding: This research was funded by National Key Research and Development Program of China (“Novel Drilling Technology Combining Ultra-high Pressure Jet and Percussion for ROP Improvement in deep geothermal drilling”, grant no. 2021YFE0111400), the Open Fund of State Key Laboratory of Shale Oil and Gas Enrichment Mechanisms and Effective Development, and the General Project of Jiangsu Province University Basic Science (NATURAL SCIENCE) Research (grant no. 22KJD430001).

Institutional Review Board Statement: The authors declare that they have no known competing financial interests or personal relationships that could have appeared to influence the work reported in this paper.

Data Availability Statement: Data will be made available on request.

Conflicts of Interest: The authors declare no conflict of interest.

References

1. Li, C.; Liu, J.; Wang, S.; Guo, Y.; Han, X.; Li, Q.; Cheng, Y.; Dong, Z.; Li, X.; Zhang, X. Numerical insights into factors affecting collapse behavior of horizontal wellbore in clayey silt hydrate-bearing sediments and the accompanying control strategy. *Ocean Eng.* **2024**, *297*, 117029. [[CrossRef](#)]
2. Li, Q.; Wang, F.; Wang, Y.; Bai, B.; Zhang, J.; Cao, L.; Sun, Q.; Wang, Y.; Forson, K. Adsorption behavior and mechanism analysis of siloxane thickener for CO₂ fracturing fluid on shallow shale soil. *J. Mol. Liq.* **2023**, *376*, 121394. [[CrossRef](#)]
3. Chen, C.; Feng, A.; Wei, Y.; Wang, Y.; Pan, X.; Song, X. Effects of WC particles on microstructure and wear behavior of laser cladding Ni60 composite coatings. *Opt. Laser Technol.* **2023**, *163*, 109425. [[CrossRef](#)]
4. Wang, Q.; Chen, F.Q.; Li, Q.; Zhang, L.; Jin, H.; Zhang, J.W. Microstructure and properties of Ni60 alloy coating prepared by electromagnetic compound field assisted laser cladding. *Mater. Chem. Phys.* **2022**, *291*, 126678. [[CrossRef](#)]
5. Xu, S.; Cai, Q.; Li, G.; Lu, X.; Zhu, X. Effect of scanning speed on microstructure and properties of TiC/Ni60 composite coatings on Ti6Al4V alloy by laser cladding. *Opt. Laser Technol.* **2022**, *154*, 108309. [[CrossRef](#)]
6. Abbas, R.K. A review on the wear of oil drill bits (conventional and the state of the art approaches for wear reduction and quantification). *Eng. Fail. Anal.* **2018**, *90*, 554–584. [[CrossRef](#)]
7. Feng, C.; Liu, W.; Gao, D. CFD simulation and optimization of slurry erosion of PDC bits. *Powder Technol.* **2022**, *408*, 117658. [[CrossRef](#)]
8. Zhao, J.; Zhang, G.; Xu, Y.; Wang, R.; Zhou, W.; Yang, D. Experimental and theoretical evaluation of solid particle erosion in an internal flow passage within a drilling bit. *J. Pet. Sci. Eng.* **2018**, *160*, 582–596. [[CrossRef](#)]
9. Kendall, O.; Abrahams, R.; Paradowska, A.; Reid, M.; Qiu, C.; Mutton, P.; Schläfer, T.; Yan, W. Influence of multi-layer laser cladding depositions and rail curvature on residual stress in light rail components. *Eng. Fail. Anal.* **2023**, *150*, 107330. [[CrossRef](#)]
10. Zhang, W.; Shang, X.; Hu, M.; He, X.; Yang, B.; Dai, K.; Ni, X.; Lu, L.; Zhou, L.; Zhang, L.; et al. Microstructure and corrosion-wear behaviors for laser cladding repaired martensitic stainless steels using CO-based and NI-based powders. *Mater. Today Commun.* **2023**, *35*, 106287. [[CrossRef](#)]
11. Li, S.; Huang, K.; Zhang, Z.; Zheng, C.; Li, M.; Wang, L.; Wu, K.; Tan, H.; Yi, X. Wear mechanisms and micro-evaluation of WC + TiC particle-reinforced Ni-based composite coatings fabricated by laser cladding. *Mater. Charact.* **2023**, *197*, 112699. [[CrossRef](#)]
12. Stanciu, V.I.; Vitry, V.; Delaunois, F. Tungsten carbide powder obtained by direct carburization of tungsten trioxide using mechanical alloying method. *J. Alloys Compd.* **2016**, *659*, 302–308. [[CrossRef](#)]
13. Dong, D.Q.; He, Y.; Chen, X.H.; Li, H.; Shi, K.H.; Zhang, L. Effect of tungsten carbide particles on microstructure and mechanical properties of Cu alloy composite bit matrix. *J. Iron Steel Res. Int.* **2023**, *31*, 519–530. [[CrossRef](#)]
14. Wu, T.; Shi, W.; Xie, L.; Gong, M.; Huang, J.; Xie, Y.; He, K. Effects of re-melting process parameters on the forming quality of the Stellite 6/WC laser cladding layer. *Optik* **2022**, *269*, 169887. [[CrossRef](#)]
15. Chen, L.; Yu, T.; Chen, X.; Zhao, Y.; Guan, C. Process optimization, microstructure and microhardness of coaxial laser cladding TiC reinforced Ni-based composite coatings. *Opt. Laser Technol.* **2022**, *152*, 108129. [[CrossRef](#)]
16. Mao, L.; Cai, M.; Liu, Q.; Han, L. Effects of spherical WC powders on the erosion behavior of WC-Ni hardfacing used for steel body drill bit. *Surf. Coat. Technol.* **2021**, *409*, 126893. [[CrossRef](#)]
17. Inagaki, M.; Kang, F. Graphene derivatives: Graphane, fluorographene, graphene oxide, graphyne and graphdiyne. *J. Mater. Chem. A* **2014**, *2*, 13193–13206. [[CrossRef](#)]
18. Sattar, T. Current review on synthesis, composites and multifunctional properties of graphene. *Top. Curr. Chem.* **2019**, *377*, 10. [[CrossRef](#)]
19. Zhan, D.; Yan, J.X.; Ni, Z.H.; Sun, L.; Lai, L.F.; Liu, L.; Shen, Z.X. Bandgap-Opened Bilayer Graphene Approached by Asymmetrical Intercalation of Trilayer Graphene. *Small* **2015**, *11*, 1177–1182. [[CrossRef](#)]
20. Jagannadham, K. Effect of interfacial interactions on the thermal conductivity and interfacial thermal conductance in tungsten-graphene layered structure. *J. Vac. Sci. Technol. A* **2014**, *32*, 051101. [[CrossRef](#)]
21. Chen, W.F.; Schneider, J.M.; Sasaki, K.; Wang, C.H.; Schneider, J. Tungsten carbide–nitride on graphene nanoplatelets as a durable hydrogen evolution electrocatalyst. *ChemSusChem* **2014**, *7*, 2414–2418. [[CrossRef](#)]
22. Xuan, L.C.; Wang, J.S. A new type of high hardness coating for improving drill bit stability in unconventional oil and gas development. *Front. Energy Res.* **2023**, *11*, 1277648. [[CrossRef](#)]
23. Metallic Materials. Rockwell Hardness Test, Part 1: Test Method. GBT230.1-2018.
24. Quantitative Analysis of Carbide Phase in High Speed Steel by X-ray Diffraction Method. YBT5336-2006.
25. Destructive Tests on Welds in Metallic Materials—Macroscopic and Microscopic Examination of Welds. ISO 17639-2003.

Disclaimer/Publisher’s Note: The statements, opinions and data contained in all publications are solely those of the individual author(s) and contributor(s) and not of MDPI and/or the editor(s). MDPI and/or the editor(s) disclaim responsibility for any injury to people or property resulting from any ideas, methods, instructions or products referred to in the content.